



An efficient numerical method for simulating multiphase flows using a diffuse interface model



Hyun Geun Lee^a, Junseok Kim^{b,*}

^a Institute of Mathematical Sciences, Ewha W. University, Seoul 120-750, Republic of Korea

^b Department of Mathematics, Korea University, Seoul 136-713, Republic of Korea

HIGHLIGHTS

- A new diffuse interface model for multiphase flows is presented.
- Surface tension and buoyancy effects on multiphase flows are studied.
- We employ a new chemical potential that can eliminate spurious phase-field profiles.
- We consider a variable mobility to investigate the effect of the mobility on the fluid dynamics.
- We significantly improve the computational efficiency of the numerical algorithm.

ARTICLE INFO

Article history:

Received 20 May 2014

Received in revised form 21 November 2014

Available online 2 January 2015

Keywords:

Multiphase flows

Continuum surface force

Surface tension and buoyancy effects

Diffuse interface model

Navier–Stokes equations

Lagrange multiplier

ABSTRACT

This paper presents a new diffuse interface model for multiphase incompressible immiscible fluid flows with surface tension and buoyancy effects. In the new model, we employ a new chemical potential that can eliminate spurious phases at binary interfaces, and consider a phase-dependent variable mobility to investigate the effect of the mobility on the fluid dynamics. We also significantly improve the computational efficiency of the numerical algorithm by adapting the recently developed scheme for the multiphase-field equation. To illustrate the robustness and accuracy of the diffuse interface model for surface tension- and buoyancy-dominant multi-component fluid flows, we perform numerical experiments, such as equilibrium phase-field profiles, the deformation of drops in shear flow, a pressure field distribution, the efficiency of the proposed scheme, a buoyancy-driven bubble in ambient fluids, and the mixing of a six-component mixture in a gravitational field. The numerical result obtained by the present model and solution algorithm is in good agreement with the analytical solution and, furthermore, we not only remove the spurious phase-field profiles, but also improve the computational efficiency of the numerical solver.

© 2014 Elsevier B.V. All rights reserved.

1. Introduction

Multiphase flows play an important role in many scientific and engineering applications, such as extractors [1], polymer blends [2], reactors [3], separators [4], sprays [5], and microfluidic technology [6,7]. For example, emulsification is one of the most common techniques used to produce micro- or nano-scale droplets. However, conventional emulsification techniques, which use inhomogeneous extensional and shear flows to rupture droplets, generate polydisperse emulsions

* Corresponding author. Tel.: +82 2 3290 3077; fax: +82 2 929 8562.

E-mail address: cfdkim@korea.ac.kr (J. Kim).

URL: <http://math.korea.ac.kr/~cfdkim> (J. Kim).

with a wide distribution of droplet sizes. Microfluidic technology offers the capability to precisely handle small volumes of fluids and produces almost monodisperse emulsions of immiscible fluids [8]. The composition, shape, and size of emulsions are influenced by the geometry and wettability of channels, and the physical properties (e.g., density, surface tension, and viscosity) of fluids [9]. Another example from nuclear safety concerns a hypothetical severe accident in a reactor. In such a scenario, the degradation of the core can produce multiphase flows in which interfaces undergo extreme topological changes such as breakup or coalescence [10].

Various numerical methods are used for simulating multiphase flows, such as the front-tracking [11,12], immersed boundary [13], volume-of-fluid [14,15], lattice Boltzmann [16,17], level-set [18–20], and diffuse interface [10,21–32] techniques. Because of its advantage in capturing interfaces implicitly, the diffuse interface method has gained considerable attention in recent years. This method replaces sharp interfaces by thin but nonzero thickness transition regions in which the interfacial forces are smoothly distributed [33]. The basic idea is to introduce an order parameter that varies continuously over thin interfacial layers and is mostly uniform in the bulk phases. The temporal evolution of the order parameter is governed by the Cahn–Hilliard equation [34,35]. Here, we view the diffuse interface method as a computational tool, and use the surface tension force derived from the geometry of the interface.

There are numerous numerical studies on two-phase [21–23,26,29,36–44] and three-phase [10,24,25,27,28,45] fluid flows. Recently, Kim [30] proposed a generalized continuous surface tension force formulation for the phase-field model for any number of fluids. To the author's knowledge, this work was the first attempt to model surface tension effects on four-component (or more) fluid flows. A critical feature of the formulation is the incorporation of a scaled delta function $\delta(c_i, c_j) = 5c_i c_j$, where c_i and c_j are the phase variables of fluids i and j , respectively, which is the simplest form and combines two different fluids. This formulation makes it possible to model any combination of interfaces without any additional decision criteria. And, Lee and Kim [31] employed this formulation to study the effect of the surface tension parameter on the mixing dynamics of multi-component fluids in a tilted channel and found that the surface tension parameter makes the flow structures more and more coherent with increase in its value.

The purpose of this paper is to extend the previous works of Kim [30] and of Lee and Kim [31] in three important ways. First, the chemical potentials used in Refs. [30,31] generate additional spurious phases at binary interfaces. Thus, we employ a new chemical potential that can eliminate spurious phases. Second, in Refs. [30,31], the constant mobility case was only considered. Thus, we consider here a phase-dependent variable mobility to investigate the effect of the mobility on the fluid dynamics. Finally, the numerical scheme used in Ref. [30] is not practical for simulating a large number of fluid components, because the calculation of a nonlinear discrete system becomes complicated when the number of components is increased. Thus, we significantly improve the computational efficiency of the numerical solution algorithm by adapting the recently developed scheme for the multiphase-field equation [46].

This paper is organized as follows. In Section 2, we present a new diffuse interface model for the mixture of N incompressible immiscible fluids. In Section 3, a numerical solution is given. We perform some characteristic numerical experiments for multi-component fluid flows in Section 4. Conclusions are drawn in Section 5. In the Appendix, we describe a nonlinear multigrid method used to solve the nonlinear discrete system at the implicit time level.

2. A diffuse interface model for the mixture of N incompressible immiscible fluids

We consider the flow of N incompressible immiscible fluids. Let $\mathbf{c} = (c_1, c_2, \dots, c_N)$ be a vector-valued phase-field. Each order parameter c_i is the concentration of each component in the mixture. Thus, admissible states will belong to the Gibbs N -simplex

$$G := \left\{ \mathbf{c} \in \mathbb{R}^N \mid \sum_{i=1}^N c_i = 1, 0 \leq c_i \leq 1 \right\}. \quad (1)$$

Without loss of generality, we postulate that the free energy can be written as follows:

$$\mathcal{F}(\mathbf{c}) = \int_{\Omega} \left(F(\mathbf{c}) + \frac{\epsilon^2}{2} \sum_{i=1}^N |\nabla c_i|^2 \right) \mathrm{d}\mathbf{x},$$

where Ω is a bounded open subset of \mathbb{R}^d ($d = 1, 2, 3$) occupied by the system, $F(\mathbf{c}) = 0.25 \sum_{i=1}^N c_i^2 (1 - c_i)^2$, and $\epsilon > 0$ is the gradient energy coefficient. The time evolution of \mathbf{c} is governed by the gradient of the energy with respect to the \dot{H}^{-1} inner product under the additional constraint (1). This constraint has to hold everywhere at all times. In order to ensure the last constraint, we use a Lagrange multiplier β_i [27,30,31,46–54]:

$$\frac{\partial c_i}{\partial t} = \nabla \cdot \left[M(\mathbf{c}) \nabla \frac{\delta}{\delta c_i} (\mathcal{F}(\mathbf{c}) + \beta_i g(\mathbf{c})) \right], \quad (2)$$

where $M(\mathbf{c})$ is a diffusional mobility and $g(\mathbf{c}) = \int_{\Omega} \left(\sum_{j=1}^N c_j - 1 \right) \mathrm{d}\mathbf{x}$. By treating the N phases independent [48,51], Eq. (2) can be reduced to

$$\frac{\partial c_i}{\partial t} = \nabla \cdot \left[M(\mathbf{c}) \nabla \left(\frac{\delta \mathcal{F}(\mathbf{c})}{\delta c_i} + \beta_i \right) \right].$$

An evaluation of β_i is carried out by summing $\frac{\partial c_i}{\partial t}$ and setting the result to 0:

$$0 = \sum_{i=1}^N \nabla \cdot \left[M(\mathbf{c}) \nabla \left(\frac{\delta \mathcal{F}(\mathbf{c})}{\delta c_i} + \beta_i \right) \right], \quad \text{i.e.,}$$

$$\sum_{i=1}^N \beta_i = - \sum_{i=1}^N \frac{\delta \mathcal{F}(\mathbf{c})}{\delta c_i}. \quad (3)$$

The simplest expression possible for β_i is to set them all equal [27,30,46,48–50,52,54]:

$$\beta_i = - \frac{1}{N} \sum_{j=1}^N \frac{\delta \mathcal{F}(\mathbf{c})}{\delta c_j}.$$

Any form of β_i , which satisfies Eq. (3), can be used and $\beta_i = -c_i \sum_{j=1}^N \frac{\delta \mathcal{F}(\mathbf{c})}{\delta c_j}$ is used in Refs. [31,51]. However, these formulations can lead to the generation of additional spurious phases at binary interfaces (we will address this issue in Section 4.1). Models that assume all interactions occur at binary interfaces may produce incorrect triple-point morphologies [55]. In order to reduce possible spurious phase formations, we introduce a new, alternative form of β_i :

$$\beta_i = - \frac{c_i^q}{\sum_{j=1}^N c_j^q} \sum_{j=1}^N \frac{\delta \mathcal{F}(\mathbf{c})}{\delta c_j},$$

which satisfies the required condition (3):

$$\sum_{i=1}^N \beta_i = - \sum_{j=1}^N \frac{\delta \mathcal{F}(\mathbf{c})}{\delta c_j} \times \frac{1}{\sum_{j=1}^N c_j^q} \times \sum_{i=1}^N c_i^q = - \sum_{j=1}^N \frac{\delta \mathcal{F}(\mathbf{c})}{\delta c_j}.$$

Note that spurious phases at binary interfaces are dramatically reduced as q increases. The temporal evolution of c_i is given by the following convective Cahn–Hilliard equation:

$$\frac{\partial c_i}{\partial t} + \nabla \cdot (c_i \mathbf{u}) = \nabla \cdot [M(\mathbf{c}) \nabla \mu_i], \quad (4)$$

$$\mu_i = \frac{\delta \mathcal{F}(\mathbf{c})}{\delta c_i} + \beta_i, \quad \text{for } i = 1, 2, \dots, N, \quad (5)$$

where \mathbf{u} is the fluid velocity. We take a concentration dependent mobility of the form $M(\mathbf{c}) = \sum_{i < j}^N c_i c_j$ [52], which is a thermodynamically reasonable choice [56]. The natural and mass conserving boundary conditions for the N -component Cahn–Hilliard system are the zero Neumann boundary conditions:

$$\nabla c_i \cdot \mathbf{n} = \nabla \mu_i \cdot \mathbf{n} = 0 \quad \text{on } \partial \Omega, \quad (6)$$

where \mathbf{n} is the unit normal vector to the domain boundary $\partial \Omega$.

The N -component fluids are governed by the modified Navier–Stokes equations and the N -component convective Cahn–Hilliard equations:

$$\rho(\mathbf{c}) \left(\frac{\partial \mathbf{u}}{\partial t} + \mathbf{u} \cdot \nabla \mathbf{u} \right) = -\nabla p + \nabla \cdot [\eta(\mathbf{c})(\nabla \mathbf{u} + \nabla \mathbf{u}^T)] + \mathbf{S}\mathbf{F}(\mathbf{c}) + \rho(\mathbf{c})\mathbf{g}, \quad (7)$$

$$\nabla \cdot \mathbf{u} = 0, \quad (8)$$

$$\frac{\partial c_i}{\partial t} + \nabla \cdot (c_i \mathbf{u}) = \nabla \cdot [M(\mathbf{c}) \nabla \mu_i], \quad (9)$$

$$\mu_i = f(c_i) - \epsilon^2 \Delta c_i + \beta_i, \quad \text{for } i = 1, 2, \dots, N, \quad (10)$$

where $\rho(\mathbf{c})$ is the variable density, p is the pressure, $\eta(\mathbf{c})$ is the variable viscosity, $\mathbf{S}\mathbf{F}(\mathbf{c})$ is the surface tension force, $\mathbf{g} = (0, -g)$ is the gravity, $f(c_i) = c_i(c_i - 0.5)(c_i - 1)$, and $\beta_i = -\frac{c_i^q}{\sum_{j=1}^N c_j^q} \sum_{j=1}^N f(c_j)$. Here, $\rho(\mathbf{c})$ and $\eta(\mathbf{c})$ are defined as $\rho(\mathbf{c}) =$

$\sum_{i=1}^N \rho_i c_i$ and $\eta(\mathbf{c}) = \sum_{i=1}^N \eta_i c_i$, where ρ_i and η_i are the i th fluid density and viscosity, respectively. For the surface tension force $\mathbf{S}\mathbf{F}(\mathbf{c})$, when $N = 3$, we decompose the physical surface tension coefficients into phase-specific surface tension coefficients. However, for $N > 3$, the decomposition generates an over-determined system and is not uniquely defined. In order to avoid the solvability problem imposed by an over-determined system, we use the generalized continuous surface tension force formulation [30]: $\mathbf{S}\mathbf{F}(\mathbf{c}) = \sum_{i=1}^{N-1} \left(\sum_{j=i+1}^N 0.5 \sigma_{ij} [\mathbf{s}\mathbf{f}(c_i) + \mathbf{s}\mathbf{f}(c_j)] \delta(c_i, c_j) \right)$, where σ_{ij} is the physical surface tension coefficient between fluids i and j , $\mathbf{s}\mathbf{f}(c_i) = -6\sqrt{2}\epsilon \nabla \cdot (\nabla c_i / |\nabla c_i|) |\nabla c_i| \nabla c_i$, and $\delta(c_i, c_j) = 5c_i c_j$.

To make the governing equations (7)–(10) dimensionless, we choose the following definitions:

$$\mathbf{x}' = \frac{\mathbf{x}}{L_c}, \quad \mathbf{u}' = \frac{\mathbf{u}}{U_c}, \quad \rho' = \frac{\rho}{\rho_c}, \quad p' = \frac{p}{\rho_c U_c^2}, \quad \eta' = \frac{\eta}{\eta_c}, \quad \mathbf{g}' = \frac{\mathbf{g}}{g}, \quad M' = \frac{M}{M_c}, \quad \mu_i' = \frac{\mu_i}{\mu_c},$$

where the primed quantities are dimensionless, and L_c is the characteristic length, U_c is the characteristic velocity, ρ_c is the characteristic density (defined as that of fluid 1), η_c is the characteristic viscosity (defined as that of fluid 1), g is the gravitational acceleration, M_c is the characteristic mobility, and μ_c is the characteristic chemical potential. Substituting these variables into Eqs. (7)–(10) and dropping the primes, we have

$$\rho(\mathbf{c}) \left(\frac{\partial \mathbf{u}}{\partial t} + \mathbf{u} \cdot \nabla \mathbf{u} \right) = -\nabla p + \frac{1}{Re} \nabla \cdot [\eta(\mathbf{c})(\nabla \mathbf{u} + \nabla \mathbf{u}^T)] + \mathbf{SF}(\mathbf{c}) + \frac{\rho(\mathbf{c})}{Fr^2} \mathbf{g}, \quad (11)$$

$$\nabla \cdot \mathbf{u} = 0, \quad (12)$$

$$\frac{\partial c_i}{\partial t} + \nabla \cdot (c_i \mathbf{u}) = \frac{1}{Pe} \nabla \cdot [M(\mathbf{c}) \nabla \mu_i], \quad (13)$$

$$\mu_i = f(c_i) - \epsilon^2 \Delta c_i + \beta_i, \quad \text{for } i = 1, 2, \dots, N, \quad (14)$$

where $\mathbf{SF}(\mathbf{c}) = \sum_{i=1}^{N-1} \left(\sum_{j=i+1}^N 0.5[\mathbf{sf}(c_i) + \mathbf{sf}(c_j)]\delta(c_i, c_j) / We_{ij} \right)$, $\mathbf{g} = (0, -1)$, and ϵ is redefined according to the scaling. The dimensionless parameters are the Reynolds number, $Re = \rho_c U_c L_c / \eta_c$, the Weber number, $We_{ij} = \rho_c L_c U_c^2 / \sigma_{ij}$, the Froude number, $Fr = U_c / \sqrt{gL_c}$, and the diffusional Péclet number, $Pe = U_c L_c / (M_c \mu_c)$.

3. Numerical solution

Let a computational domain be uniformly partitioned with spacing h . The cell center is located at $(x_i, y_j) = ((i-0.5)h, (j-0.5)h)$ for $i = 1, \dots, N_x$ and $j = 1, \dots, N_y$. N_x and N_y are the number of cells in the x - and y -directions, respectively. Cell vertices are located at $(x_{i+\frac{1}{2}}, y_{j+\frac{1}{2}}) = (ih, jh)$. Pressures and vector-valued phase-fields are stored at cell centers, and velocities are stored at cell faces [57]. Let Δt be the time step and n be the time step index. We assume that $\sum_{k=1}^N c_k^n = 1$ by the constraint (1) for all n . At the beginning of each time step, given \mathbf{u}^n and \mathbf{c}^n , we want to find \mathbf{u}^{n+1} , \mathbf{c}^{n+1} , and p^{n+1} that solve the following discrete equations:

$$\rho^n \frac{\mathbf{u}^{n+1} - \mathbf{u}^n}{\Delta t} = -\nabla_d p^{n+1} + \frac{1}{Re} \nabla_d \cdot [\eta^n (\nabla_d \mathbf{u}^n + (\nabla_d \mathbf{u}^n)^T)] + \mathbf{SF}^n + \frac{\rho^n}{Fr^2} \mathbf{g} - \rho^n (\mathbf{u} \cdot \nabla_d \mathbf{u})^n, \quad (15)$$

$$\nabla_d \cdot \mathbf{u}^{n+1} = 0, \quad (16)$$

$$\frac{c_k^{n+1} - c_k^n}{\Delta t} = \frac{1}{Pe} \nabla_d \cdot [M^n \nabla_d \mu_k^{n+\frac{1}{2}}] - \nabla_d \cdot (c_k \mathbf{u})^n, \quad (17)$$

$$\mu_k^{n+\frac{1}{2}} = \varphi(c_k^{n+1}) - 0.25 c_k^n - \epsilon^2 \Delta_d c_k^{n+1} + \beta_k^n, \quad \text{for } k = 1, 2, \dots, N-1, \quad (18)$$

where $\rho^n = \rho(\mathbf{c}^n)$, $\eta^n = \eta(\mathbf{c}^n)$, $\mathbf{SF}^n = \mathbf{SF}(\mathbf{c}^n)$, $M^n = M(\mathbf{c}^n)$, and $\varphi(c_k) = f(c_k) + 0.25 c_k$ is a nonlinear function. Note that we need only solve these equations with c_1^{n+1} , c_2^{n+1} , \dots , c_{N-1}^{n+1} , because $c_N^{n+1} = 1 - \sum_{k=1}^{N-1} c_k^{n+1}$. The main procedure for solving Eqs. (15)–(18) in each time step is as follows.

Step 1. Initialize \mathbf{u}^0 to be the divergence-free velocity field and c_k^0 for $k = 1, 2, \dots, N-1$.

Step 2. An intermediate velocity field, $\tilde{\mathbf{u}}$, is calculated without the pressure gradient term:

$$\frac{\tilde{\mathbf{u}} - \mathbf{u}^n}{\Delta t} = \frac{1}{\rho^n Re} \nabla_d \cdot [\eta^n (\nabla_d \mathbf{u}^n + (\nabla_d \mathbf{u}^n)^T)] + \frac{1}{\rho^n} \mathbf{SF}^n + \frac{\mathbf{g}}{Fr^2} - (\mathbf{u} \cdot \nabla_d \mathbf{u})^n,$$

where the convective term, $(\mathbf{u} \cdot \nabla_d \mathbf{u})^n$, is computed using an upwind scheme [58]. The following pressure Poisson equation is then solved by a linear multigrid method [59] to obtain the pressure needed to enforce incompressibility:

$$\nabla_d \cdot \left(\frac{1}{\rho^n} \nabla_d p^{n+1} \right) = \frac{1}{\Delta t} \nabla_d \cdot \tilde{\mathbf{u}}.$$

Then we obtain the divergence-free velocity field: $\mathbf{u}^{n+1} = \tilde{\mathbf{u}} - \frac{\Delta t}{\rho^n} \nabla_d p^{n+1}$.

Step 3. Update the phase-field c_k^n to c_k^{n+1} for $k = 1, 2, \dots, N-1$ [46]. This step is described in the Appendix. Note that, for mass conservation, we use a conservative discretization of the convective part of the phase-field equation (17):

$$[(c_k u)_x + (c_k v)_y]_{ij}^n = \frac{u_{i+\frac{1}{2},j}^n (c_{k,i+1,j}^n + c_{k,i,j}^n) - u_{i-\frac{1}{2},j}^n (c_{k,i,j}^n + c_{k,i-1,j}^n)}{2h} + \frac{v_{i,j+\frac{1}{2}}^n (c_{k,i,j+1}^n + c_{k,i,j}^n) - v_{i,j-\frac{1}{2}}^n (c_{k,i,j}^n + c_{k,i,j-1}^n)}{2h}.$$

These complete the one time step.

4. Numerical experiments

We perform numerical experiments to illustrate the robustness and accuracy of the diffuse interface model for multi-component fluid flows. In our numerical experiments, for simplicity of notation, we define the functions $d(x, y; a, b, r)$, $l(x; a)$, and $l(y; b)$, respectively, as

$$d(x, y; a, b, r) := \frac{1}{2} \left(1 + \tanh \left(\frac{r - \sqrt{(x-a)^2 + (y-b)^2}}{2\sqrt{2}\epsilon} \right) \right),$$

$$l(x; a) := \frac{1}{2} \left(1 + \tanh \left(\frac{x-a}{2\sqrt{2}\epsilon} \right) \right), \quad \text{and} \quad l(y; b) := \frac{1}{2} \left(1 + \tanh \left(\frac{y-b}{2\sqrt{2}\epsilon} \right) \right).$$

4.1. Comparison between three different chemical potentials – equilibrium phase-field profiles

As mentioned in Section 2, the previous chemical potentials, $\mu_i = \frac{\delta \mathcal{F}(\mathbf{c})}{\delta c_i} - \frac{1}{N} \sum_{j=1}^N \frac{\delta \mathcal{F}(\mathbf{c})}{\delta c_j}$ [30] and $\mu_i = \frac{\delta \mathcal{F}(\mathbf{c})}{\delta c_i} - c_i \sum_{j=1}^N \frac{\delta \mathcal{F}(\mathbf{c})}{\delta c_j}$ [31,51], lead to the generation of additional spurious phases at binary interfaces. In order to confirm this, we consider the equilibrium of three drops placed within another fluid. We use the N -component convective Cahn–Hilliard equations (9) and (10) with zero velocity $\mathbf{u} = \mathbf{0}$. And we consider the constant mobility ($M(\mathbf{c}) \equiv 1$) to focus on the effect of chemical potential. The initial conditions are

$$c_1(x, y, 0) = d(x, y; 0.25, 0.25, 0.1), \quad (19)$$

$$c_2(x, y, 0) = d(x, y; 0.5, 0.75, 0.1), \quad (20)$$

$$c_3(x, y, 0) = d(x, y; 0.75, 0.25, 0.1) \quad (21)$$

on the domain $\Omega = [0, 1] \times [0, 1]$. Here, we use $\epsilon = 0.0075$, $h = 1/128$, and $\Delta t = 10h$. We continue the computation until the solution becomes numerically stationary.

Fig. 1(a), (c), and (e) shows the numerical equilibrium profiles of c_1 , c_2 , and c_3 with the first previous [30], second previous [31,51], and new ($\mu_i = \frac{\delta \mathcal{F}(\mathbf{c})}{\delta c_i} - \frac{c_i^q}{\sum_{j=1}^N c_j^q} \sum_{j=1}^N \frac{\delta \mathcal{F}(\mathbf{c})}{\delta c_j}$ with $q = 2$) chemical potentials, respectively. Note that the second previous chemical potential can be considered as $q = 1$ in the new chemical potential. Fig. 1(b), (d), and (f) shows additional phases in each equilibrium state in Fig. 1(a), (c), and (e), respectively. When using a diffuse interface model, even though the order parameter c_i is conserved globally, c_i shifts slightly from its expected values in the bulk phases [60]. Because of this phenomenon, we may observe the generation of additional spurious phases at binary interfaces in the bulk phases of c_i . For c_1 , the first previous chemical potential μ_1 is

$$\mu_1 = \frac{3}{4}f(c_1) - \epsilon^2 \Delta c_1 - \frac{1}{4}(f(c_2) + f(c_3) + f(c_4)).$$

The term $-\frac{1}{4}(f(c_2) + f(c_3) + f(c_4))$ acts on not only the interface of c_1 but also the bulk phases (see Fig. 2(a)) and thus makes c_1 appear in the bulk phases. As a result, after a sufficiently large time, we observe that a significant amount of the phase c_1 appears between the phase c_2 and c_3 interface. Likewise, the phase c_2 appears between the phase c_1 and c_3 interface, and the phase c_3 appears between the phase c_1 and c_2 interface. For the case of second previous chemical potential, μ_1 is

$$\mu_1 = (1 - c_1)f(c_1) - \epsilon^2 \Delta c_1 - c_1(f(c_2) + f(c_3) + f(c_4))$$

and the term $-c_1(f(c_2) + f(c_3) + f(c_4))$ is about two orders of magnitude smaller than the term $-\frac{1}{4}(f(c_2) + f(c_3) + f(c_4))$ in the first previous chemical potential (see Fig. 2(b)). Thus, the generation of additional spurious phases is more suppressed than using the first previous chemical potential. On the other hand, with the new chemical potential with $q = 2$, μ_1 is

$$\mu_1 = \left(1 - \frac{c_1^2}{c_1^2 + c_2^2 + c_3^2 + c_4^2} \right) f(c_1) - \epsilon^2 \Delta c_1 - \frac{c_1^2}{c_1^2 + c_2^2 + c_3^2 + c_4^2} (f(c_2) + f(c_3) + f(c_4))$$

and the term $-\frac{c_1^2}{c_1^2 + c_2^2 + c_3^2 + c_4^2} (f(c_2) + f(c_3) + f(c_4))$ is about two orders of magnitude smaller than the term $-c_1(f(c_2) + f(c_3) + f(c_4))$ in the second previous chemical potential (see Fig. 2(c)). As a result, after a sufficiently large time, there are nearly no spurious phases at binary interfaces.

We also test with $q = 3$. Fig. 3(a) and (b) shows the numerical equilibrium profiles of c_1 , c_2 , and c_3 and additional phases in each equilibrium state in (a), respectively. The term $-\frac{c_1^3}{c_1^3 + c_2^3 + c_3^3 + c_4^3} (f(c_2) + f(c_3) + f(c_4))$ in the new chemical potential with $q = 3$ in the bulk phases of c_1 is shown in Fig. 3(c). From Figs. 1(c)–(f), 2, and 3, we conclude that the generation of additional spurious phases can be more suppressed as q increases. For more than $q = 2$, the result is marginally improved and thus we will use $q = 2$ in the remaining sections.

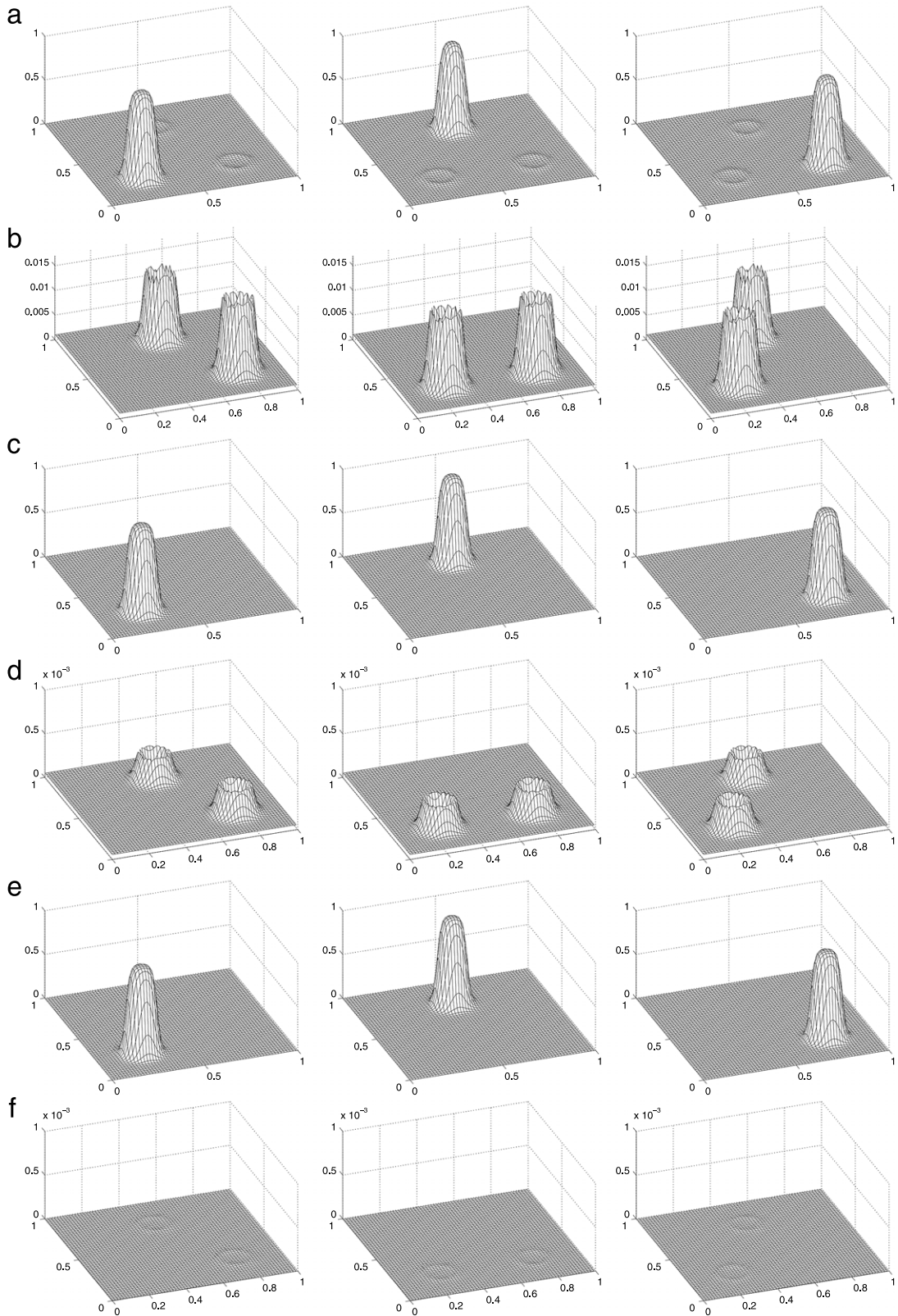


Fig. 1. (a), (c), and (e) show equilibrium states obtained with the first previous [30], second previous [31,51], and new chemical potentials, respectively. (b), (d), and (f) show additional phases in each equilibrium state in (a), (c), and (e), respectively. The left, middle, and right columns correspond to c_1 , c_2 , and c_3 , respectively. The new chemical potential, $\mu_i = \frac{\delta \mathcal{F}(\mathbf{c})}{\delta c_i} - \frac{c_i^q}{\sum_{j=1}^N c_j^q} \sum_{j=1}^N \frac{\delta \mathcal{F}(\mathbf{c})}{\delta c_j}$ with $q = 2$, generates nearly no spurious additional phases at binary phases.

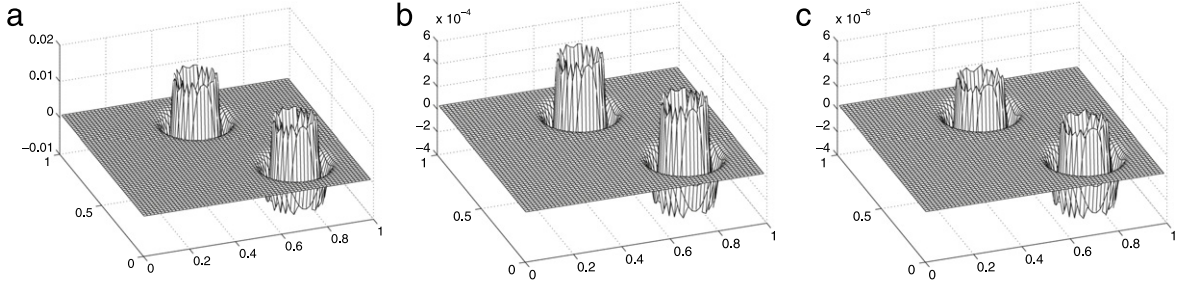


Fig. 2. (a), (b), and (c) show the terms $-\frac{1}{4}(f(c_2) + f(c_3) + f(c_4))$ (in the first previous chemical potential), $-c_1(f(c_2) + f(c_3) + f(c_4))$ (in the second previous chemical potential), and $-\frac{c_1^2}{c_1^2+c_2^2+c_3^2+c_4^2}(f(c_2) + f(c_3) + f(c_4))$ (in the new chemical potential with $q = 2$) in the bulk phases of c_1 , respectively.

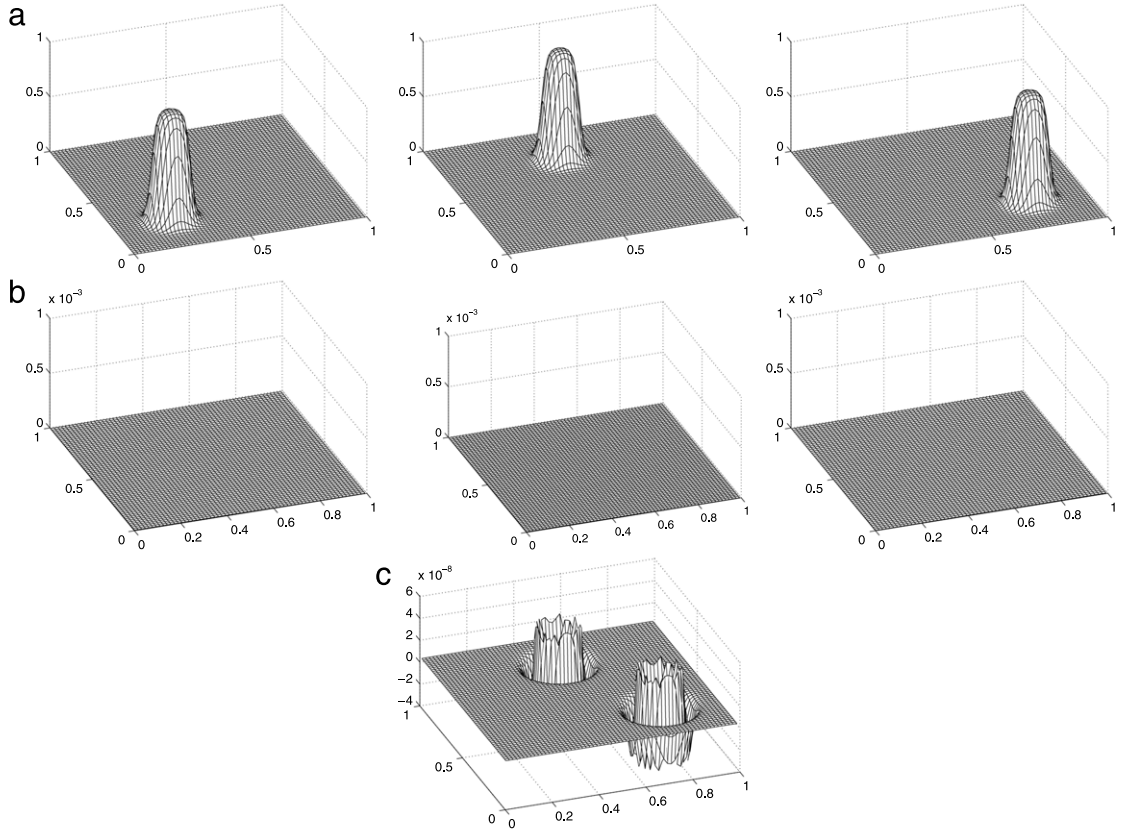


Fig. 3. (a) and (b) show equilibrium states obtained with the new chemical potential with $q = 3$ and additional phases in each equilibrium state in (a), respectively. The left, middle, and right columns correspond to c_1 , c_2 , and c_3 , respectively. (c) shows the term $-\frac{c_1^3}{c_1^3+c_2^3+c_3^3+c_4^3}(f(c_2) + f(c_3) + f(c_4))$ in the new chemical potential with $q = 3$ in the bulk phases of c_1 .

4.2. Comparison between constant and variable mobilities

In this section, we demonstrate the fundamental difference between constant ($M(\mathbf{c}) \equiv 1$) and variable ($M(\mathbf{c}) = \sum_{i < j}^N c_i c_j$) mobilities. The reduction of the total amount of interfacial area is the main driving force in the Cahn–Hilliard system for both constant and variable mobilities. In the case of variable mobility this is done only by local adjustment in connected phase regions, whereas in the case of constant mobility also nonlocal interactions are used to achieve this. To show the difference between constant and variable mobilities under shear flow, we take the initial conditions and the velocity as

$$\begin{aligned} c_1(x, y, 0) &= d(x, y; 0.8, 0.7, 0.15) + d(x, y; 1.2, 0.7, 0.15), \\ c_2(x, y, 0) &= d(x, y; 0.8, 0.3, 0.15), \\ c_3(x, y, 0) &= d(x, y; 1.2, 0.3, 0.15), \\ u(x, y, t) &= 2(y - 0.5), \quad v(x, y, t) = 0 \end{aligned}$$

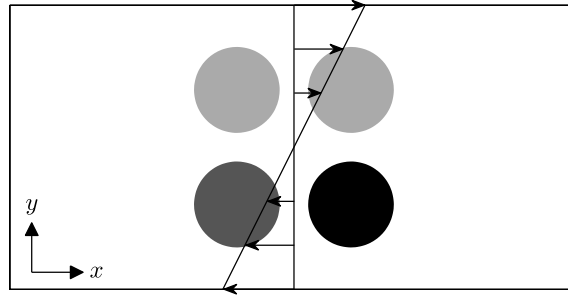


Fig. 4. Schematic illustration of drops in shear flow.

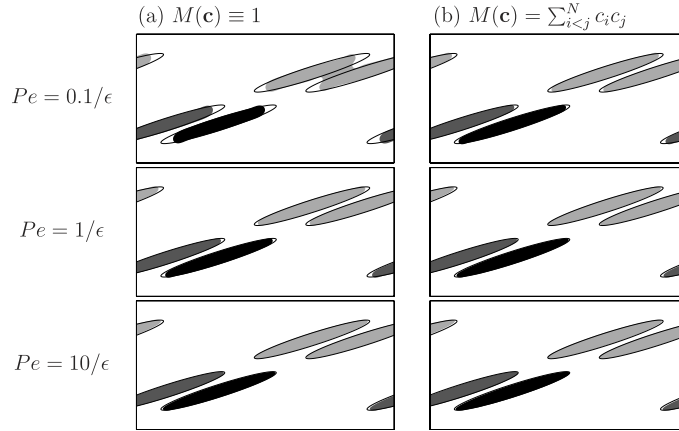


Fig. 5. Drop deformation in shear flow with (a) constant and (b) variable mobilities at $t = 1.41$.

on the domain $\Omega = [0, 2] \times [0, 1]$ (see Fig. 4). We use the N -component convective Cahn–Hilliard equations (13) and (14) (the drops are simply advected by the shear flow). We choose $\epsilon = 0.006$, $h = 1/128$, and $\Delta t = 0.01h$, and vary the Péclet number; $Pe = 0.1/\epsilon$, $1/\epsilon$, and $10/\epsilon$.

Fig. 5(a) and (b) shows the deformation of drops in shear flow with constant and variable mobilities, respectively. In Fig. 5, solid lines represent the exact interfaces. In the case of constant mobility, when $Pe = 0.1/\epsilon$ is relatively small (the diffusion term in Eq. (13) is relatively dominant), two drops (c_1) do not follow the flow faithfully, and collide and coalesce since the bulk diffusion is still possible and disconnected phase regions influence each other. However, the drops follow the flow well as the Péclet number increases. Furthermore, it is observed that the interfacial transition region is uniform for not only $Pe = 0.1/\epsilon$ but also $1/\epsilon$ (we can see that the interfacial transition region is nonuniform on the tips of drops when $Pe = 10/\epsilon$, see Fig. 6(a)). Note that the advection term in Eq. (13) becomes dominant as the Péclet number increases and this implies that the interfaces are locally out of equilibrium. In the case of variable mobility, two drops (c_1) follow the flow faithfully for all $Pe = 0.1/\epsilon$, $1/\epsilon$, and $10/\epsilon$. However, the interfacial transition region is uniform for only $Pe = 0.1/\epsilon$ (see Fig. 6(b)). Therefore, in this test, considering both uniform interfacial transition and interface profile according to the flow, $Pe = 1/\epsilon$ and $0.1/\epsilon$ are appropriate for constant and variable mobilities, respectively.

4.3. Pressure field distribution—mesh refinement study

In order to demonstrate the present model's ability to calculate the pressure field directly from the governing equations, we consider the equilibrium of a drop-in-drop-in-drop placed within another fluid (see Fig. 7(a)). At the equilibrium, if there are no external forces, the velocity vanishes ($\mathbf{u} = \mathbf{0}$) and the pressures are uniform in each phase. The pressure jump between two phases is given by Laplace's formula [61]

$$p_i - p_j = \sigma_{ij} \kappa_{ij} = \frac{\sigma_{ij}}{r_{ij}},$$

where σ_{ij} , κ_{ij} , and r_{ij} are the surface tension coefficient, the curvature, and the radius of the interface between phases i and j , respectively. The initial conditions are

$$c_1(x, y, 0) = d(x, y; 0.5, 0.5, 0.1),$$

$$c_2(x, y, 0) = d(x, y; 0.5, 0.5, 0.2) - c_1(x, y, 0),$$

$$c_3(x, y, 0) = d(x, y; 0.5, 0.5, 0.3) - c_1(x, y, 0) - c_2(x, y, 0)$$

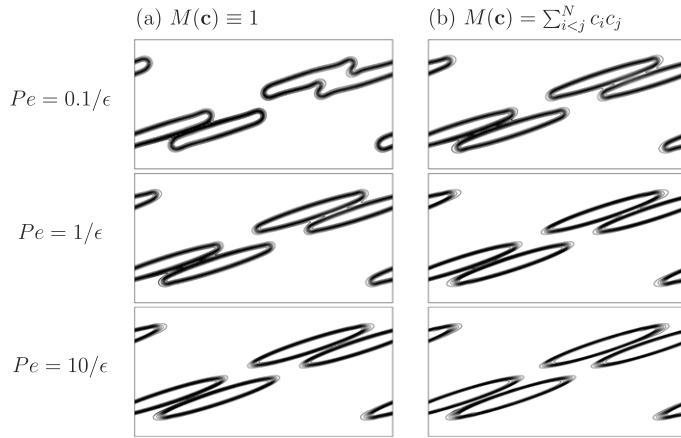


Fig. 6. Contour lines of the order parameters c_1 , c_2 , and c_3 in Fig. 5 at levels 0.1, 0.2, . . . , 0.9.

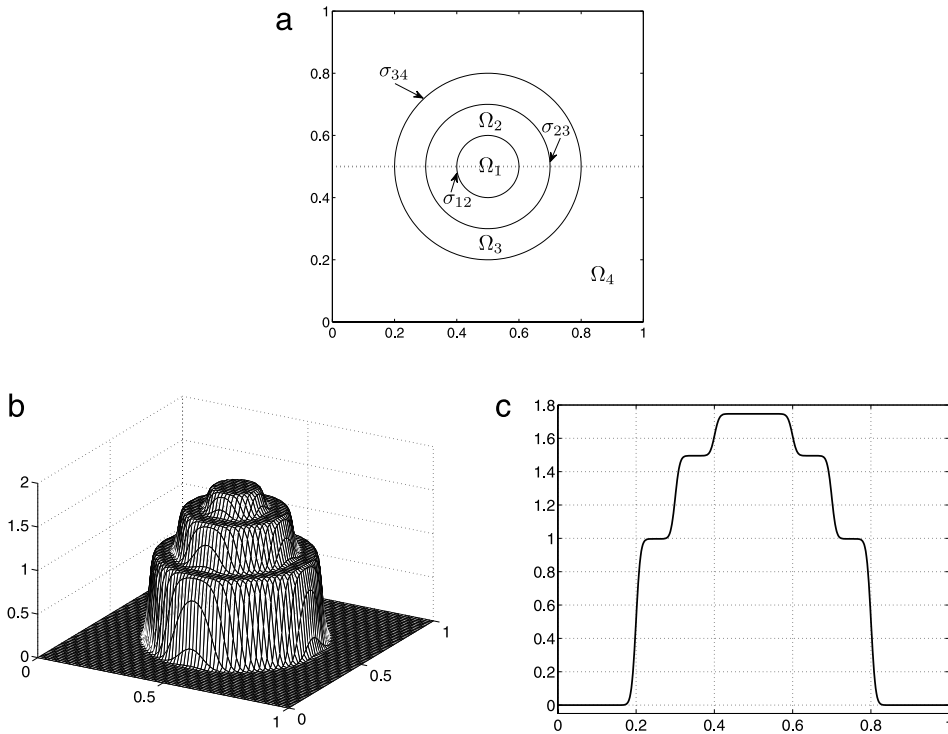


Fig. 7. (a) Schematic illustration of a drop-in-drop-in-drop placed within another fluid. (b) Pressure field for the three drops. (c) Slice of the pressure field at $y = 0.5$ (dotted line in (a)).

on the domain $\Omega = [0, 1] \times [0, 1]$. Eq. (7) becomes $\nabla p = \mathbf{SF}(\mathbf{c})$ and thus we solve $\Delta p = \nabla \cdot \mathbf{SF}(\mathbf{c})$ with $\epsilon = 0.01$ and the uniform grids $h = 1/2^n$ for $n = 6, 7, 8$, and 9 . The surface tensions are $\sigma_{12} = 0.025$, $\sigma_{23} = 0.1$, $\sigma_{34} = 0.3$, and $\sigma_{13} = \sigma_{14} = \sigma_{24} = 1$.

Table 1 shows the convergence of the pressure jump as we refine the mesh size. Fig. 7(b) and (c) shows the pressure field for the three drops and the pressure jumps along the line $y = 0.5$, respectively. From Table 1 and Fig. 7(b) and (c), we can see that the present model enables the accurate calculation of the pressure field for multi-component fluid flows.

4.4. Efficiency of the proposed scheme

In order to show the efficiency of the proposed scheme, we consider the phase separation of $N = 3, \dots, 10$ components on the domain $\Omega = [0, 1] \times [0, 1]$. For each number of components, the initial conditions are randomly chosen rectangles. The initial velocity is zero and the fluids are density- and viscosity-matched ($\rho_i = \eta_i = 1$ for $i = 1, \dots, N$). We choose

Table 1

Numerical pressure jump when refining the mesh size. The theoretical pressure jump is 1.75.

Mesh size (h)	1/64	1/128	1/256	1/512
Numerical pressure jump	1.5405	1.6900	1.7319	1.7426

Table 2

Average CPU times (s) for different number of components.

N	3	4	5	6	7	8	9	10
Average CPU time	1.234	1.815	2.473	2.973	3.612	4.203	4.721	5.331

Table 3

Average CPU times (s) of the previous and present algorithms for $N = 4, 5,$ and 6 .

N	4	5	6
Previous algorithm	2.611	14.463	105.791
Present algorithm	1.815	2.473	2.973

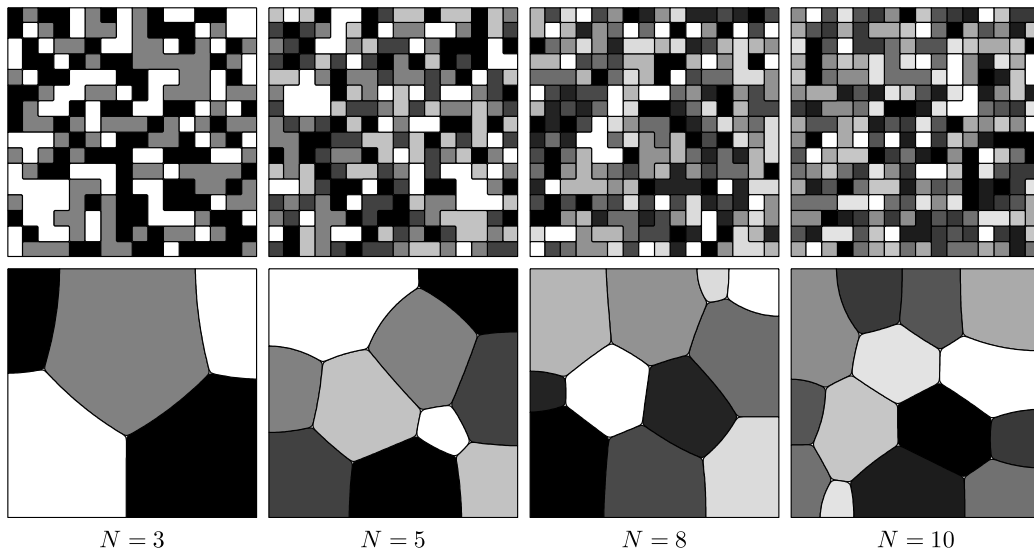


Fig. 8. Phase separation of $N = 3, 5, 8,$ and 10 components. The top and bottom rows correspond to $t = 0$ and $t = 50,000\Delta t$, respectively.

$\epsilon = 0.0042$, $h = 1/128$, $\Delta t = 0.1h$, $Re = 100$, $Pe = 1$, and $We_{ij} = 100$. Simulations are run for 50,000 time steps and performed on Intel Core i3 CPU 550 @ 3.20 GHz processor and 2GB RAM. In this test, the effect of gravity is neglected.

The evolution of the interface is shown in Fig. 8. The top and bottom rows correspond to $t = 0$ and $t = 50,000\Delta t$, respectively. Table 2 lists the average CPU time (in seconds) over the 50,000 time steps for each number of components. Note that the average CPU time includes the time for solving the modified Navier–Stokes equations (11) and (12). In this paper, most of terms in Eqs. (11) and (12) are calculated explicitly and we use a linear multigrid method to solve the pressure Poisson equation. However, the time for solving the pressure Poisson equation is negligible compared to the time for solving the N -component convective Cahn–Hilliard equations (13) and (14). We apply a nonlinear multigrid method $N - 1$ times to solve Eqs. (13) and (14) and this step (Step 3 in Section 3) is dominant for the CPU time. The time for solving the modified Navier–Stokes equations accounts for about 5 to 8% of the CPU time. The results in Table 2 suggest that the convergence rate of the average CPU time is linear with respect to the number of components.

Note that the previous work [30] has a practical limitation: the calculation of a nonlinear discrete system becomes complicated as the number of components increases because, in the FAS multigrid cycle, one SMOOTH relaxation operator step consists of solving the system with a $2(N - 1) \times 2(N - 1)$ coefficient matrix for each i and j . However, in the present work, we only need to solve the system with a 2×2 coefficient matrix $N - 1$ times for each i and j . In order to compare previous and present algorithms, we measure the CPU time of the previous algorithm for the above problem. Table 3 provides the average CPU time (in seconds) of the previous and present algorithms over 50,000 time steps for $N = 4, 5,$ and 6 . The present algorithm reaches the final time step in a much smaller CPU time.

4.5. Numerical simulation of a buoyancy-driven bubble

In this section, the buoyancy-driven evolution of a bubble is investigated. When a buoyancy-driven bubble crosses a horizontal fluid–fluid interface, the bubble can either penetrate the interface and rise into the upper fluid layer, or remain captured between the two fluid layers. Fig. 9 shows a schematic illustration of the initial configuration. The initial conditions and the initial velocity are

$$\begin{aligned} c_1(x, y, 0) &= d(x, y; 0.5, 0.4, 0.2), \\ c_2(x, y, 0) &= 1 - l(y; 0.8) - c_1(x, y, 0), \\ c_3(x, y, 0) &= l(y; 0.8) - l(y; 2.5), \\ u(x, y, 0) &= v(x, y, 0) = 0 \end{aligned}$$

on the domain $\Omega = [0, 1] \times [0, 4]$. Parameter values of $\epsilon = 0.006\sqrt{2}$, $h = 1/64$, and $\Delta t = 0.05h$ are used. We take the viscosities of the components to be matched ($\eta_1 = \eta_2 = \eta_3 = \eta_4 = 1$) with the following parameters:

$$\begin{aligned} \rho_1 = 1, \quad \rho_2 = 4, \quad \rho_3 = 3, \quad \rho_4 = 2, \quad Re = 30, \quad Fr = 1, \quad Pe = 0.01/\epsilon, \\ We_{12} = 30, \quad We_{13} = 20, \quad We_{23} = 15, \quad We_{24} = 1, \quad We_{34} = 60. \end{aligned}$$

For We_{14} , we employ two different values, $We_{14} = 40$ and 10 . No-slip boundary conditions are applied at the top and bottom walls, and periodic boundary conditions are used at the side boundaries.

Fig. 10(a) and (b) shows the evolution of the bubble obtained with $We_{14} = 40$ and 10 at the same times, respectively. The Weber number, which relates to the relative magnitude of inertial and surface tension forces at the interface, is expected to influence the simulation results of buoyancy-driven bubbles. In each figure, fluid 1 is represented by the white region, fluid 2 by the black region, fluid 3 by the dark gray region, and fluid 4 by the gray region. Until $t = 13.28$, both cases show similar behavior: a very thin film of fluid 2 covers the top part of the bubble ($t = 2.34$). When the bubble is no longer immersed in fluid 2, the departure of the bubble becomes visible ($t = 5.46$). After the bubble crosses the interface between fluids 2 and 3, the rising bubble again reaches a fluid–fluid interface ($t = 13.28$). After $t = 13.28$, in the case of $We_{14} = 40$, we can again observe the departure and rising of the bubble. However, in the case of $We_{14} = 10$, the bubble remains trapped at the fluid–fluid interface, and cannot rise into the upper fluid layer because the surface tension force is greater than the buoyancy force. See Ref. [62] for the theoretical criterion and experimental results of the bubble entrainment phenomenon, and also refer to Ref. [10] for numerical studies of entrainment in a ternary fluid system.

We also simulate the case of non-equal viscosities; $\eta_1 = 1$, $\eta_2 = 1$, $\eta_3 = 0.5$, and $\eta_4 = 0.25$. In this simulation, we take the same initial conditions, initial velocity, and parameter values used to create Fig. 10(a). Fig. 11 shows the evolution of the bubble obtained with the non-equal viscosities. Until $t = 2.34$, the behavior of the bubble in Fig. 11 is similar to that in Fig. 10(a). After the bubble crosses the interface between fluids 2 and 3, the bubble rises more rapidly and is more flattened than the bubble in Fig. 10(a) because of the contrast of viscosity.

4.6. Mixing of a six-component mixture in a gravitational field—rising bubble, falling drop, and the Rayleigh–Taylor instability

In order to model the mixing of a six-component mixture in a gravitational field, we take the initial conditions as shown in the first snapshot of Fig. 12 and the initial velocity as zero:

$$\begin{aligned} c_1(x, y, 0) &= l(y; 2.5) - d(x, y; 0.25, 2.75, 0.15) + d(x, y; 0.75, 0.25, 0.15), \\ c_2(x, y, 0) &= l(y; 2) - l(y; 2.5), \\ c_3(x, y, 0) &= l(y; 1) - l(y; 1.5 + 0.1 \cos(2\pi x)), \\ c_4(x, y, 0) &= l(y; 1.5 + 0.1 \cos(2\pi x)) - l(y; 2), \\ c_5(x, y, 0) &= l(y; 0.5) - l(y; 1), \\ u(x, y, 0) &= v(x, y, 0) = 0 \end{aligned}$$

on the domain $\Omega = [0, 1] \times [0, 3]$. For $i = 1, \dots, 6$, $\rho_i = i$ and $\eta_i = 1$. Parameter values of $\epsilon = 0.006\sqrt{2}$, $h = 1/64$, and $\Delta t = 0.1h$ are used. The dimensionless parameters are $Re = 100$, $Fr = 1$, $Pe = 0.01/\epsilon$, $We_{16} = 10$, $We_{15} = We_{26} = 15$, $We_{14} = We_{36} = 20$, $We_{13} = We_{46} = 25$, $We_{12} = We_{24} = We_{25} = We_{35} = We_{56} = 30$, and $We_{23} = We_{34} = We_{45} = 50$. No-slip boundary conditions are applied at the top and bottom walls, and periodic boundary conditions are employed at the side boundaries. As we can see in the first snapshot of Fig. 12, in the middle of the domain (between $y = 1$ and $y = 2$), a heavy fluid is superposed over a light fluid. The interface between the two fluids is unstable, and any perturbation of the interface tends to grow with time, producing the phenomenon known as the Rayleigh–Taylor instability [63,64]. This phenomenon leads to the penetration of both the heavy and light fluids into each other.

Fig. 12 shows the evolution of the six-component mixture system in a gravitational field. In Fig. 12, we can see various phenomena caused by a density contrast: a rising bubble, a falling drop, and the Rayleigh–Taylor instability. The results in Fig. 12 demonstrate that the present model and solution algorithm can handle complex interactions between many components.

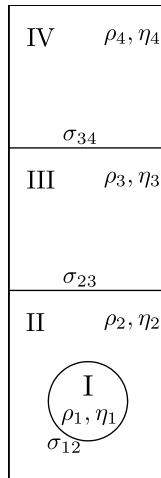


Fig. 9. Schematic illustration of the initial configuration.

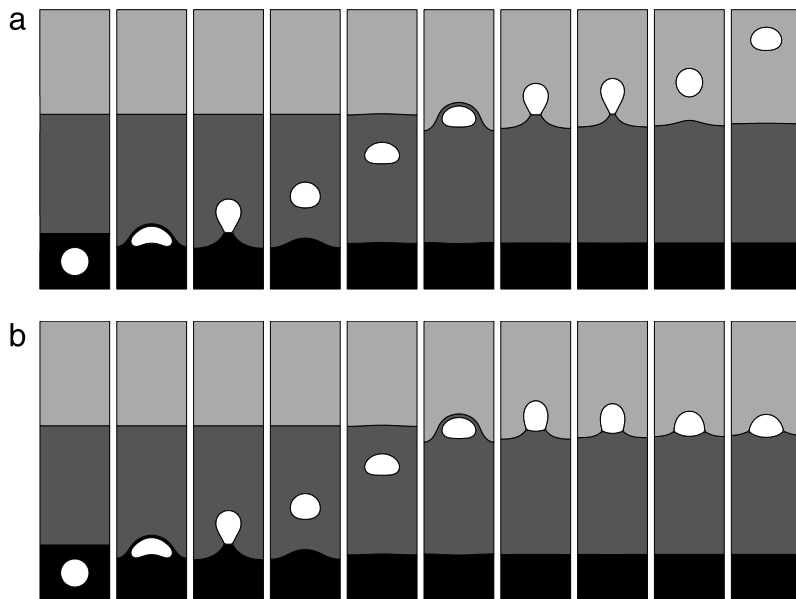


Fig. 10. Buoyancy-driven bubble crossing a fluid–fluid interface with two different values (a) $We_{14} = 40$ and (b) $We_{14} = 10$. The times are $t = 0, 2.34, 5.46, 7.03, 10.15, 13.28, 16.40, 17.18, 18.75,$ and 23.43 (from left to right). The other Weber numbers are $We_{12} = 30, We_{13} = 20, We_{23} = 15, We_{24} = 1,$ and $We_{34} = 60$.

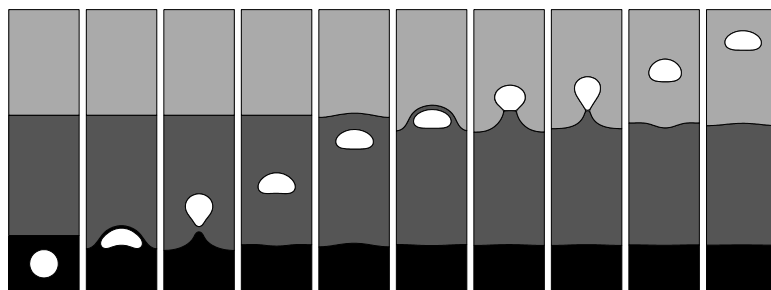


Fig. 11. Buoyancy-driven bubble crossing a fluid–fluid interface with the non-equal viscosities; $\eta_1 = 1, \eta_2 = 1, \eta_3 = 0.5,$ and $\eta_4 = 0.25$. The times are $t = 0, 2.34, 5.46, 7.03, 10.15, 11.71, 14.06, 14.84, 16.40,$ and 18.75 (from left to right).

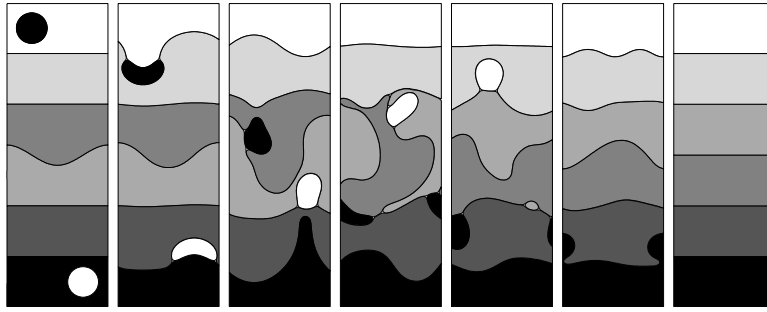


Fig. 12. Rising bubble, falling drop, and the Rayleigh–Taylor instability. The times are $t = 0, 1.56, 4.68, 7.81, 10.93, 14.06,$ and 39.06 (from left to right).

Table 4

Numerical pressure jump when refining the mesh size. The theoretical pressure jump is 1.75.

Mesh size (h)	1/64	1/128	1/256	1/512
Numerical pressure jump	1.7314	1.6900	1.7011	1.7172

4.7. Pressure field distribution—alternative surface tension force formulation

In the present model, we use $\mathbf{sf}(c_i)\delta(c_i, c_j) = -30\sqrt{2}\epsilon \nabla \cdot \left(\frac{\nabla c_i}{|\nabla c_i|} \right) \frac{\nabla c_j}{|\nabla c_j|} |\nabla c_i|^2 c_i c_j$ as in Ref. [30]. For $\mathbf{sf}(c_i)\delta(c_i, c_j)$, there are many other expressions we can use [65]. One of them is as follows: $\mathbf{sf}(c_i)\delta(c_i, c_j) = -\frac{1}{\sqrt{2}\epsilon^2} \epsilon \nabla \cdot \left(\frac{\nabla c_i}{|\nabla c_i|} \right) \frac{\nabla c_j}{|\nabla c_j|} c_i c_j$. Note that $\frac{1}{\sqrt{2}\epsilon^2} \epsilon c_i c_j$ has a wider support than $30\sqrt{2}\epsilon |\nabla c_i|^2 c_i c_j$. For this alternative expression, we perform the problem presented in Section 4.3. Table 4 shows the convergence of the pressure jump as we refine the mesh size. From Table 4, we can see that the alternative expression also enables the accurate calculation of the pressure field for multi-component fluid flows.

4.8. Comparison between two different variable mobilities—equilibrium phase-field profiles

In Eq. (9), we consider the variable mobility $M(\mathbf{c}) = \sum_{i < j}^N c_i c_j$ which is same for all order parameters. We can also consider a variable mobility $M_i = c_i(1 - c_i)$, which is different for each order parameter, instead of $M(\mathbf{c})$. To compare the effect of two different variable mobilities, we take the initial conditions as

$$c_1(x, y, 0) = d(x, y; 0.5, 0.5, 0.15),$$

$$c_2(x, y, 0) = d(x, y; 1, 1.5, 0.15),$$

$$c_3(x, y, 0) = d(x, y; 1.5, 0.5, 0.15)$$

on the domain $\Omega = [0, 2] \times [0, 2]$. Here, we use $\epsilon = 0.0075$, $h = 1/128$, and $\Delta t = 10h$. We solve the N -component convective Cahn–Hilliard equations with zero velocity $\mathbf{u} = \mathbf{0}$ and continue the computation until the solution becomes numerically stationary. Fig. 13(a) and (c) shows the numerical equilibrium profiles of c_1 , c_2 , and c_3 with $M(\mathbf{c}) = \sum_{i < j}^N c_i c_j$ and $M_i = c_i(1 - c_i)$, respectively. Fig. 13(b) and (d) shows additional phases in each equilibrium state in Fig. 13(a) and (c), respectively. We observe that a variable mobility $M_i = c_i(1 - c_i)$ reduces the generation of additional spurious phases more effectively.

5. Conclusions

We presented a new diffuse interface model for multi-component incompressible immiscible fluid flows with surface tension and buoyancy effects. In the new model, we employed a new chemical potential that can eliminate spurious phases at binary interfaces, and considered a phase-dependent variable mobility to investigate the effect of the mobility on the fluid dynamics. We also significantly improved the computational efficiency of the numerical algorithm by adapting the recently developed scheme for the multiphase-field equation. The numerical result obtained by the present model and solution algorithm was in good agreement with the analytical solution and, furthermore, we not only removed the spurious phase-field profiles, but also improved the computational efficiency of the numerical solver. In particular, the average CPU time is linear with respect to the number of components. And we investigated the difference between constant and variable mobilities by varying the Péclet number on the simulation of deformation of drops in shear flow. Applying various Weber numbers, we observed buoyancy-driven bubbles that can penetrate the interface and rise into the upper fluid layer, or remain captured between two fluid layers by the balance between buoyancy and surface tension forces. Also, by modeling

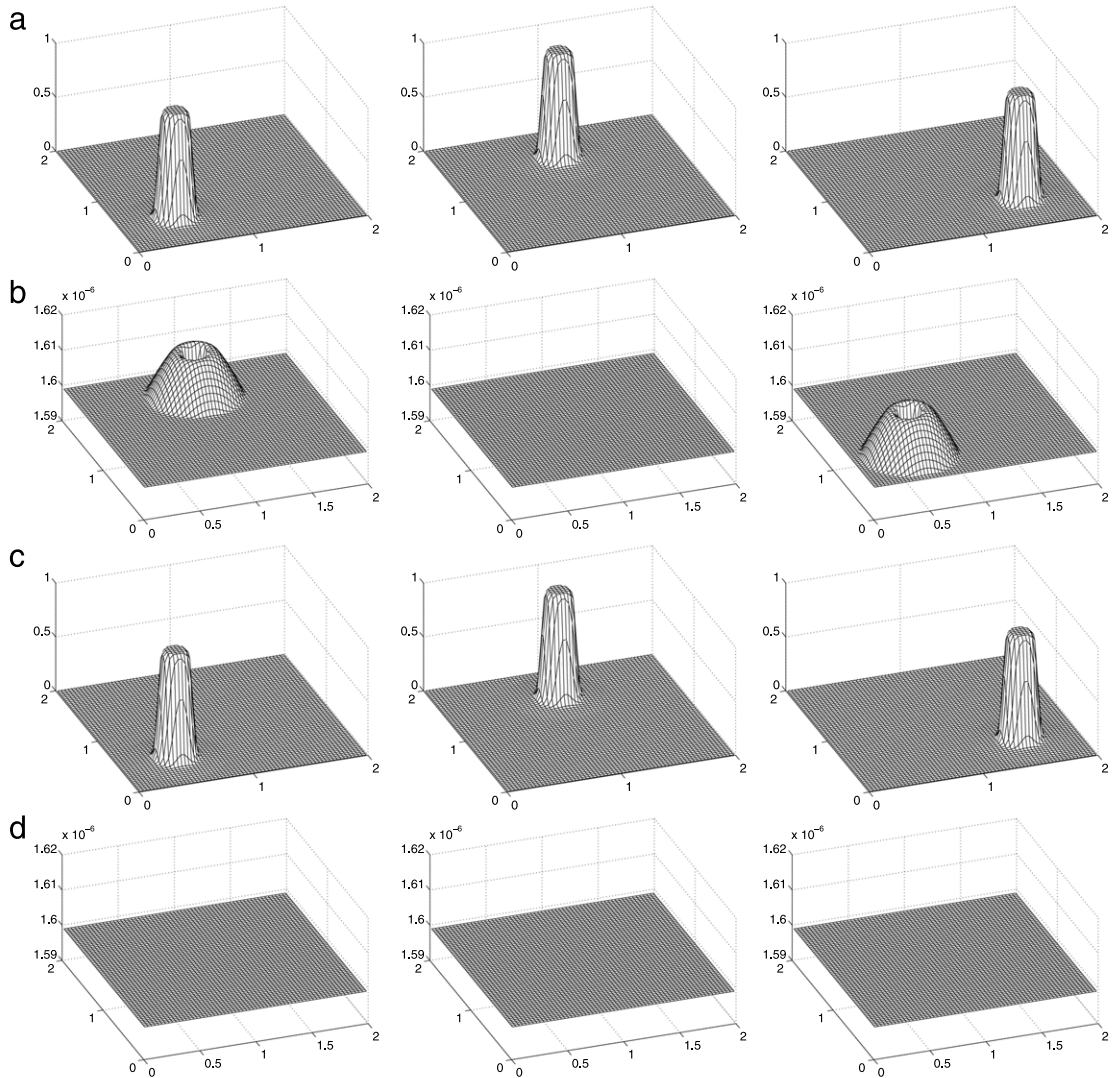


Fig. 13. (a) and (c) show equilibrium states obtained with $M(\mathbf{c}) = \sum_{i < j}^N c_i c_j$ and $M_i = c_i(1 - c_i)$, respectively. (b) and (d) show additional phases in each equilibrium state in (a) and (c), respectively. The left, middle, and right columns correspond to c_1 , c_2 , and c_3 , respectively.

a six-component mixture in a gravitational field, we simulated various phenomena caused by a density contrast: a rising bubble, a falling drop, and the Rayleigh–Taylor instability. The results demonstrate that the present model and solution algorithm can handle complex interactions between many components. In future work, we will apply the present model and solution algorithm to predict the formation of double emulsions in a capillary microfluidic device [66] which was observed experimentally by Utada et al. [8].

Acknowledgments

The first author (H.G. Lee) was supported by Basic Science Research Program through the National Research Foundation of Korea (NRF) funded by the Ministry of Education (2009-0093827). The corresponding author (J. Kim) thanks the reviewers for the constructive and helpful comments on the revision of this article.

Appendix

In this section, we describe a nonlinear Full Approximation Storage (FAS) multigrid method to solve the nonlinear discrete system (17) and (18) at the implicit time level. The nonlinearity, $\varphi(c_k)$, is treated using one step of Newton's iteration and a pointwise Gauss–Seidel relaxation scheme is used as the smoother in the multigrid method.

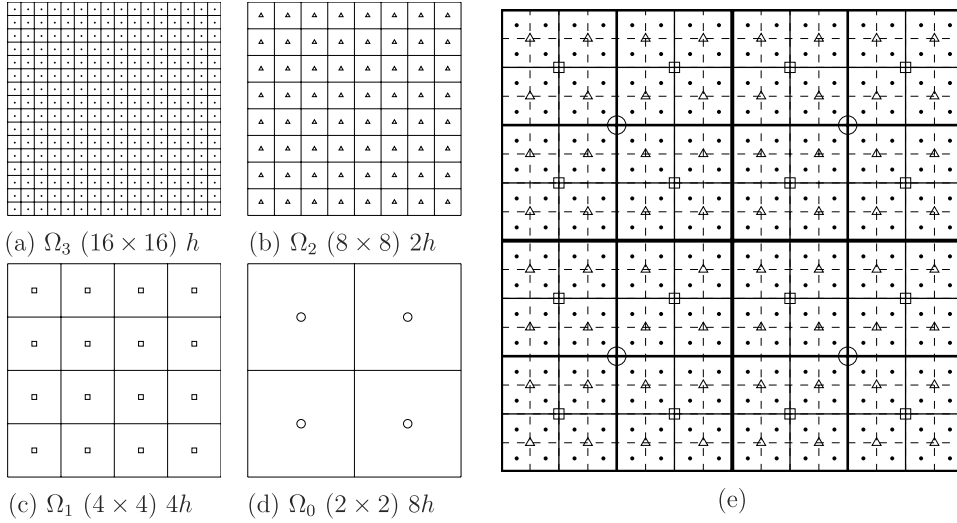


Fig. 14. (a), (b), (c), and (d) are a sequence of coarse grids for $N_x = N_y = 16$ ($L = 3$). (e) is a composition of grids, Ω_3 , Ω_2 , Ω_1 , and Ω_0 .

Let Eqs. (17) and (18) be $N(c_k^{n+1}, \mu_k^{n+\frac{1}{2}}) = (\phi^n, \psi^n)$, where the nonlinear operator (N) is defined as

$$N(c_k^{n+1}, \mu_k^{n+\frac{1}{2}}) = \left(\frac{c_k^{n+1}}{\Delta t} - \frac{1}{Pe} \nabla_d \cdot \left[M^n \nabla_d \mu_k^{n+\frac{1}{2}} \right], \mu_k^{n+\frac{1}{2}} - \varphi(c_k^{n+1}) + \epsilon^2 \Delta_d c_k^{n+1} \right)$$

and the source term is $(\phi^n, \psi^n) = (c_k^n / \Delta t - \nabla_d \cdot (c_k \mathbf{u})^n, -0.25c_k^n + \beta_k^n)$.

Let L satisfy $N_x = s_1 \cdot 2^{L+1}$ and $N_y = s_2 \cdot 2^{L+1}$ for odd numbers s_1 and s_2 . Then, we define a sequence of coarser and coarser grids

$$\Omega_l = \{(x_{l,i} = (i - 0.5)h_l, y_{l,j} = (j - 0.5)h_l) \mid i = 1, \dots, N_x/2^{L-l}, j = 1, \dots, N_y/2^{L-l}, h_l = h \cdot 2^{L-l}\}$$

for $l = L, \dots, 0$. Ω_L and Ω_0 are the finest and coarsest grids, respectively, and Ω_{l-1} is coarser than Ω_l by a factor of 2. Fig. 14 shows a schematic of a sequence of coarse grids for $N_x = N_y = 16$ ($L = 3$). In the following description of one FAS cycle, we use the subscript l to denote the functions and operators on Ω_l grid, assume the number ν of pre- and post-smoothing relaxation sweeps to be fixed, and start on the finest grid $l = L$. We set the initial guess $\{c_{k,L}^{n+1,0}, \mu_{k,L}^{n+\frac{1}{2},0}\} = \{c_k^n, \mu_k^{n-\frac{1}{2}}\}$ and calculate $\{c_{k,l}^{n+1,m+1}, \mu_{k,l}^{n+\frac{1}{2},m+1}\}$ from the given $\{c_{k,l}^{n+1,m}, \mu_{k,l}^{n+\frac{1}{2},m}\}$ for $m = 0, 1, \dots$, where $\{c_{k,l}^{n+1,m}, \mu_{k,l}^{n+\frac{1}{2},m}\}$ and $\{c_{k,l}^{n+1,m+1}, \mu_{k,l}^{n+\frac{1}{2},m+1}\}$ are the approximations of $\{c_{k,l}^{n+1}, \mu_{k,l}^{n+\frac{1}{2}}\}$ before and after one FAS cycle, respectively. We iterate the FAS cycle until a maximum norm of the consecutive error $\|c_{k,L}^{n+1,m+1} - c_{k,L}^{n+1,m}\|_\infty$ is less than a tolerance and then we set $\{c_k^{n+1}, \mu_k^{n+\frac{1}{2}}\} = \{c_{k,L}^{n+1,m+1}, \mu_{k,L}^{n+\frac{1}{2},m+1}\}$.

An iteration step for the nonlinear multigrid method using the V-cycle is as follows:

FAS multigrid cycle

$$\{c_{k,l}^{n+1,m+1}, \mu_{k,l}^{n+\frac{1}{2},m+1}\} = \text{FAScycle}(l, c_{k,l}^{n+1,m}, \mu_{k,l}^{n+\frac{1}{2},m}, N_l, \phi_l^n, \psi_l^n, \nu) \text{ on } \Omega_l \text{ grid.}$$

Now, we define the FAS cycle which comprises the pre-smoothing, coarse-grid correction, and post-smoothing steps.

(1) Pre-smoothing

Compute $\{\bar{c}_{k,l}^{n+1,m}, \bar{\mu}_{k,l}^{n+\frac{1}{2},m}\}$ by applying ν smoothing steps to $\{c_{k,l}^{n+1,m}, \mu_{k,l}^{n+\frac{1}{2},m}\}$

$$\{\bar{c}_{k,l}^{n+1,m}, \bar{\mu}_{k,l}^{n+\frac{1}{2},m}\} = \text{SMOOTH}^\nu(c_{k,l}^{n+1,m}, \mu_{k,l}^{n+\frac{1}{2},m}, N_l, \phi_l^n, \psi_l^n) \text{ on } \Omega_l \text{ grid.}$$

First, let us discretize Eq. (17) as a Gauss–Seidel type: for $s = 0, \dots, \nu - 1$,

$$\begin{aligned} \frac{c_{k,l,ij}^{s+1}}{\Delta t} + \frac{M_{l,i+\frac{1}{2},j}^n + M_{l,i-\frac{1}{2},j}^n + M_{l,i,j+\frac{1}{2}}^n + M_{l,i,j-\frac{1}{2}}^n}{h_l^2 Pe} \mu_{k,l,ij}^{s+1} &= \phi_{l,ij}^n \\ + \frac{M_{l,i+\frac{1}{2},j}^n \mu_{k,l,i+1,j}^s + M_{l,i-\frac{1}{2},j}^n \mu_{k,l,i-1,j}^{s+1} + M_{l,i,j+\frac{1}{2}}^n \mu_{k,l,i,j+1}^s + M_{l,i,j-\frac{1}{2}}^n \mu_{k,l,i,j-1}^{s+1}}{h_l^2 Pe}, \end{aligned} \tag{22}$$

where $M_{l,i+\frac{1}{2},j}^n = M(0.5(\mathbf{c}_{l,i+1,j}^n + \mathbf{c}_{l,ij}^n))$ and the other terms are similarly defined. Here, $\{c_{k,l,ij}^0, \mu_{k,l,ij}^0\} = \{c_{k,l,ij}^{n+1,m}, \mu_{k,l,ij}^{n+\frac{1}{2},m}\}$, and $\{c_{k,l,ij}^s, \mu_{k,l,ij}^s\}$ and $\{c_{k,l,ij}^{s+1}, \mu_{k,l,ij}^{s+1}\}$ are the approximations of $\{\bar{c}_{k,l,ij}^{n+1,m}, \bar{\mu}_{k,l,ij}^{n+\frac{1}{2},m}\}$ before and after one smoothing step, respectively. Next, let us discretize Eq. (18). Because $\varphi(c_{k,l,ij}^{s+1})$ is nonlinear with respect to $c_{k,l,ij}^{s+1}$, we linearize $\varphi(c_{k,l,ij}^{s+1})$ at $c_{k,l,ij}^s$, i.e.,

$$\varphi(c_{k,l,ij}^{s+1}) \approx \varphi(c_{k,l,ij}^s) + (c_{k,l,ij}^{s+1} - c_{k,l,ij}^s) \frac{\partial \varphi(c_{k,l,ij}^s)}{\partial c_k} \tag{23}$$

Then, putting Eq. (23) into Eq. (18) yields

$$-c_{k,l,ij}^{s+1} \left(\frac{\partial \varphi(c_{k,l,ij}^s)}{\partial c_k} + \frac{4\epsilon^2}{h_l^2} \right) + \mu_{k,l,ij}^{s+1} = \psi_{l,ij}^n + \varphi(c_{k,l,ij}^s) - c_{k,l,ij}^s \frac{\partial \varphi(c_{k,l,ij}^s)}{\partial c_k} - \frac{\epsilon^2}{h_l^2} (c_{k,l,i+1,j}^s + c_{k,l,i-1,j}^{s+1} + c_{k,l,i,j+1}^s + c_{k,l,i,j-1}^{s+1}). \tag{24}$$

One SMOOTH relaxation operator step consists of solving the system (22) and (24) by a 2×2 matrix inversion for each i and j :

$$\begin{pmatrix} a_{11} & a_{12} \\ a_{21} & a_{22} \end{pmatrix} \begin{pmatrix} c_{k,l,ij}^{s+1} \\ \mu_{k,l,ij}^{s+1} \end{pmatrix} = \begin{pmatrix} \bar{\phi}_{l,ij}^n \\ \bar{\psi}_{l,ij}^n \end{pmatrix}, \tag{25}$$

where $a_{11} = 1/\Delta t$, $a_{12} = (M_{l,i+\frac{1}{2},j}^n + M_{l,i-\frac{1}{2},j}^n + M_{l,i,j+\frac{1}{2}}^n + M_{l,i,j-\frac{1}{2}}^n)/(h_l^2 Pe)$, $a_{21} = -\partial \varphi(c_{k,l,ij}^s)/\partial c_k - 4\epsilon^2/h_l^2$, $a_{22} = 1$, and the right-hand side of Eq. (25) is the right-hand side terms in Eqs. (22) and (24). After applying ν smoothing steps (when $s = \nu - 1$), we set $\{\bar{c}_{k,l,ij}^{n+1,m}, \bar{\mu}_{k,l,ij}^{n+\frac{1}{2},m}\} = \{c_{k,l,ij}^\nu, \mu_{k,l,ij}^\nu\}$.

(2) Coarse-grid correction

(2.1) Compute the defect : $(\bar{d}_{1,l}^m, \bar{d}_{2,l}^m) = (\phi_{l,ij}^n, \psi_{l,ij}^n) - N_l(\bar{c}_{k,l}^{n+1,m}, \bar{\mu}_{k,l}^{n+\frac{1}{2},m})$.

(2.2) Restrict the defect and $\{\bar{c}_{k,l}^{n+1,m}, \bar{\mu}_{k,l}^{n+\frac{1}{2},m}\}$:

$$(\bar{d}_{1,l-1}^m, \bar{d}_{2,l-1}^m, \bar{c}_{k,l-1}^{n+1,m}, \bar{\mu}_{k,l-1}^{n+\frac{1}{2},m}) = I_l^{l-1}(\bar{d}_{1,l}^m, \bar{d}_{2,l}^m, \bar{c}_{k,l}^{n+1,m}, \bar{\mu}_{k,l}^{n+\frac{1}{2},m}).$$

The restriction operator I_l^{l-1} maps l -level functions to $(l-1)$ -level functions:

$$\begin{aligned} \bar{d}_{1,l-1}^m(x_{l-1,i}, y_{l-1,j}) &= I_l^{l-1} \bar{d}_{1,l}^m(x_{l-1,i}, y_{l-1,j}) \\ &= \frac{1}{4} \left[\bar{d}_{1,l}^m \left(x_{l-1,i} - \frac{h_l}{2}, y_{l-1,j} - \frac{h_l}{2} \right) + \bar{d}_{1,l}^m \left(x_{l-1,i} + \frac{h_l}{2}, y_{l-1,j} - \frac{h_l}{2} \right) \right. \\ &\quad \left. + \bar{d}_{1,l}^m \left(x_{l-1,i} - \frac{h_l}{2}, y_{l-1,j} + \frac{h_l}{2} \right) + \bar{d}_{1,l}^m \left(x_{l-1,i} + \frac{h_l}{2}, y_{l-1,j} + \frac{h_l}{2} \right) \right] \end{aligned}$$

for a coarse-grid point $(x_{l-1,i}, y_{l-1,j}) \in \Omega_{l-1}$. That is, coarse-grid values are obtained by averaging the four nearby fine-grid values. The other terms are similarly defined.

(2.3) Compute the right-hand side :

$$(\phi_{l-1}^n, \psi_{l-1}^n) = (\bar{d}_{1,l-1}^m, \bar{d}_{2,l-1}^m) + N_{l-1}(\bar{c}_{k,l-1}^{n+1,m}, \bar{\mu}_{k,l-1}^{n+\frac{1}{2},m}).$$

(2.4) Compute an approximate solution $\{\hat{c}_{k,l-1}^{n+1,m}, \hat{\mu}_{k,l-1}^{n+\frac{1}{2},m}\}$ of the coarse-grid equation on Ω_{l-1} :

$$N_{l-1}(\hat{c}_{k,l-1}^{n+1,m}, \hat{\mu}_{k,l-1}^{n+\frac{1}{2},m}) = (\phi_{l-1}^n, \psi_{l-1}^n). \tag{26}$$

If $l = 1$, we apply the SMOOTH relaxation operator. If $l > 1$, we solve Eq. (26) by performing an FAS l -grid cycle using $\{\bar{c}_{k,l-1}^{n+1,m}, \bar{\mu}_{k,l-1}^{n+\frac{1}{2},m}\}$ as an initial approximation:

$$\{\hat{c}_{k,l-1}^{n+1,m}, \hat{\mu}_{k,l-1}^{n+\frac{1}{2},m}\} = \text{FAScycle}(l-1, \bar{c}_{k,l-1}^{n+1,m}, \bar{\mu}_{k,l-1}^{n+\frac{1}{2},m}, N_{l-1}, \phi_{l-1}^n, \psi_{l-1}^n, \nu).$$

(2.5) Compute the coarse-grid correction (CGC) :

$$\hat{w}_{1,l-1}^{n+1,m} = \hat{c}_{k,l-1}^{n+1,m} - \bar{c}_{k,l-1}^{n+1,m}, \quad \hat{w}_{2,l-1}^{n+\frac{1}{2},m} = \hat{\mu}_{k,l-1}^{n+\frac{1}{2},m} - \bar{\mu}_{k,l-1}^{n+\frac{1}{2},m}.$$

(2.6) Interpolate the correction : $(\hat{w}_{1,l}^{n+1,m}, \hat{w}_{2,l}^{n+\frac{1}{2},m}) = I_{l-1}(\hat{w}_{1,l-1}^{n+1,m}, \hat{w}_{2,l-1}^{n+\frac{1}{2},m})$.

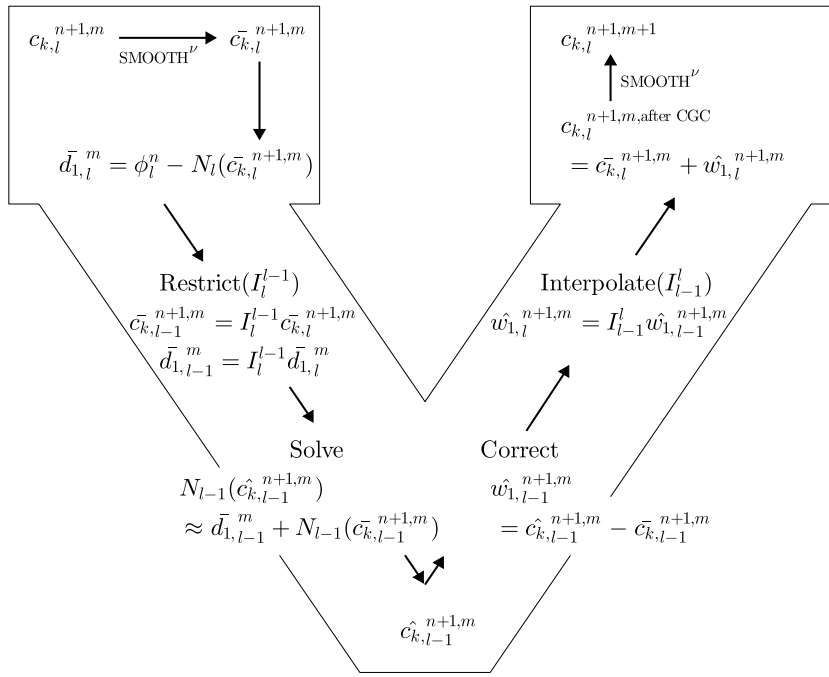


Fig. 15. FAS ($l, l - 1$) two-grid method.

The interpolation operator I_{l-1}^l maps $(l - 1)$ -level functions to l -level functions. Here, the coarse values are simply transferred to the four nearby fine-grid points, i.e., $\hat{w}_{1,l}^{n+1,m} \left(x_{l-1,i} - \frac{h_l}{2}, y_{l-1,j} - \frac{h_l}{2} \right) = \hat{w}_{1,l}^{n+1,m} \left(x_{l-1,i} + \frac{h_l}{2}, y_{l-1,j} - \frac{h_l}{2} \right) = \hat{w}_{1,l}^{n+1,m} \left(x_{l-1,i} - \frac{h_l}{2}, y_{l-1,j} + \frac{h_l}{2} \right) = \hat{w}_{1,l}^{n+1,m} \left(x_{l-1,i} + \frac{h_l}{2}, y_{l-1,j} + \frac{h_l}{2} \right) = \hat{w}_{1,l-1}^{n+1,m}(x_{l-1,i}, y_{l-1,j})$ for a coarse-grid point $(x_{l-1,i}, y_{l-1,j}) \in \Omega_{l-1}$. The other term is similarly defined.

(2.7) Compute the corrected approximation on Ω_l :

$$c_{k,l}^{n+1,m, \text{after CGC}} = \bar{c}_{k,l}^{n+1,m} + \hat{w}_{1,l}^{n+1,m}, \quad \mu_{k,l}^{n+\frac{1}{2},m, \text{after CGC}} = \bar{\mu}_{k,l}^{n+\frac{1}{2},m} + \hat{w}_{2,l}^{n+\frac{1}{2},m}.$$

(3) Post-smoothing

Compute $\{c_{k,l}^{n+1,m+1}, \mu_{k,l}^{n+\frac{1}{2},m+1}\}$ by applying ν smoothing steps to $\{c_{k,l}^{n+1,m, \text{after CGC}}, \mu_{k,l}^{n+\frac{1}{2},m, \text{after CGC}}\}$

$$\{c_{k,l}^{n+1,m+1}, \mu_{k,l}^{n+\frac{1}{2},m+1}\} = \text{SMOOTH}^\nu(c_{k,l}^{n+1,m, \text{after CGC}}, \mu_{k,l}^{n+\frac{1}{2},m, \text{after CGC}}, N_l, \phi_l^n, \psi_l^n) \text{ on } \Omega_l \text{ grid.}$$

This completes the description of a nonlinear FAS cycle. Fig. 15 shows a schematic diagram of the FAS cycle.

References

- [1] R. Rieger, C. Weiss, G. Wigley, H.-J. Bart, R. Marr, Investigating the process of liquid–liquid extraction by means of computational fluid dynamics, *Comput. Chem. Eng.* 20 (1996) 1467–1475.
- [2] C.L. Tucker, P. Moldenaers, Microstructural evolution in polymer blends, *Annu. Rev. Fluid Mech.* 34 (2002) 177–210.
- [3] S. Sundaresan, Modeling the hydrodynamics of multiphase flow reactors: current status and challenges, *AIChE J.* 46 (2000) 1102–1105.
- [4] C.T. Crowe, J.D. Schwarzkopf, M. Sommerfeld, Y. Tsuji, *Multiphase Flows with Droplets and Particles*, CRC Press, FL, 2012.
- [5] J.K. Dukowicz, A particle–fluid numerical model for liquid sprays, *J. Comput. Phys.* 35 (1980) 229–253.
- [6] M. De Menech, Modeling of droplet breakup in a microfluidic T-shaped junction with a phase–field model, *Phys. Rev. E* 73 (2006) 031505.
- [7] L. Ménétrier-Deremble, P. Tabeling, Droplet breakup in microfluidic junctions of arbitrary angles, *Phys. Rev. E* 74 (2006) 035303.
- [8] A.S. Utada, E. Lorenceau, D.R. Link, P.D. Kaplan, H.A. Stone, D.A. Weitz, Monodisperse double emulsions generated from a microcapillary device, *Science* 308 (2005) 537–541.
- [9] L. Shui, J.C.T. Eijkel, A. van den Berg, Multiphase flow in microfluidic systems – control and applications of droplets and interfaces, *Adv. Colloid Interface Sci.* 133 (2007) 35–49.
- [10] F. Boyer, C. Lapuerta, S. Minjeaud, B. Piar, M. Quintard, Cahn–Hilliard/Navier–Stokes model for the simulation of three-phase flows, *Transp. Porous Media* 82 (2010) 463–483.
- [11] S.O. Unverdi, G. Tryggvason, A front-tracking method for viscous, incompressible, multi-fluid flows, *J. Comput. Phys.* 100 (1992) 25–37.
- [12] G. Tryggvason, B. Bunner, A. Esmaeili, D. Juric, N. Al-Rawahi, W. Tauber, J. Han, S. Nas, Y.-J. Jan, A front-tracking method for the computations of multiphase flow, *J. Comput. Phys.* 169 (2001) 708–759.
- [13] H.S. Udaykumar, H.-C. Kan, W. Shyy, R. Tran-Son-Tay, Multiphase dynamics in arbitrary geometries on fixed cartesian grids, *J. Comput. Phys.* 137 (1997) 366–405.
- [14] E.G. Puckett, A.S. Almgren, J.B. Bell, D.L. Marcus, W.J. Rider, A high-order projection method for tracking fluid interfaces in variable density incompressible flows, *J. Comput. Phys.* 130 (1997) 269–282.

- [15] D. Gueyffier, J. Li, A. Nadim, R. Scardovelli, S. Zaleski, Volume-of-fluid interface tracking with smoothed surface stress methods for three-dimensional flows, *J. Comput. Phys.* 152 (1999) 423–456.
- [16] S. Foroughi, S. Jamshidi, M. Masihi, Lattice Boltzmann method on quadtree grids for simulating fluid flow through porous media: a new automatic algorithm, *Phys. A* 392 (2013) 4772–4786.
- [17] A. Karimipour, M.H. Esfe, M.R. Safaei, D.T. Semiromi, S. Jafari, S.N. Kazi, Mixed convection of copper–water nanofluid in a shallow inclined lid driven cavity using the lattice Boltzmann method, *Phys. A* 402 (2014) 150–168.
- [18] Y.C. Chang, T.Y. Hou, B. Merriman, S. Osher, A level set formulation of Eulerian interface capturing methods for incompressible fluid flows, *J. Comput. Phys.* 124 (1996) 449–464.
- [19] V. Sochnikov, S. Efrima, Level set calculations of the evolution of boundaries on a dynamically adaptive grid, *Internat. J. Numer. Methods Engrg.* 56 (2003) 1913–1929.
- [20] P. Gómez, J. Hernández, J. López, On the reinitialization procedure in a narrow-band locally refined level set method for interfacial flows, *Internat. J. Numer. Methods Engrg.* 63 (2005) 1478–1512.
- [21] C. Liu, J. Shen, A phase field model for the mixture of two incompressible fluids and its approximation by a Fourier-spectral method, *Physica D* 179 (2003) 211–228.
- [22] P. Yue, J.J. Feng, C. Liu, J. Shen, A diffuse-interface method for simulating two-phase flows of complex fluids, *J. Fluid Mech.* 515 (2004) 293–317.
- [23] V.V. Khatavkar, P.D. Anderson, P.C. Duineveld, H.H.E. Meijer, Diffuse interface modeling of droplet impact on a pre-patterned solid surface, *Macromol. Rapid Commun.* 26 (2005) 298–303.
- [24] J. Kim, J. Lowengrub, Phase field modeling and simulation of three-phase flows, *Interface Free Bound.* 7 (2005) 435–466.
- [25] F. Boyer, C. Lapuerta, Study of a three component Cahn–Hilliard flow model, *ESAIM: M2AN* 40 (2006) 653–687.
- [26] V.V. Khatavkar, P.D. Anderson, H.H.E. Meijer, Capillary spreading of a droplet in the partially wetting regime using a diffuse-interface model, *J. Fluid Mech.* 572 (2007) 367–387.
- [27] J. Kim, Phase field computations for ternary fluid flows, *Comput. Methods Appl. Mech. Engrg.* 196 (2007) 4779–4788.
- [28] F. Boyer, S. Minjeaud, Numerical schemes for a three component Cahn–Hilliard model, *ESAIM: M2AN* 45 (2011) 697–738.
- [29] H.G. Lee, J. Kim, Accurate contact angle boundary conditions for the Cahn–Hilliard equations, *Comput. Fluids* 44 (2011) 178–186.
- [30] J. Kim, A generalized continuous surface tension force formulation for phase-field models for multi-component immiscible fluid flows, *Comput. Methods Appl. Mech. Engrg.* 198 (2009) 3105–3112.
- [31] H.G. Lee, J. Kim, Buoyancy-driven mixing of multi-component fluids in two-dimensional tilted channels, *Eur. J. Mech. B Fluids* 42 (2013) 37–46.
- [32] J. Li, Q. Wang, A class of conservative phase field models for multiphase fluid flows, *J. Appl. Mech.* 81 (2014) 021004.
- [33] V.E. Badalassi, H.D. Ceniceros, S. Banerjee, Computation of multiphase systems with phase field models, *J. Comput. Phys.* 190 (2003) 371–397.
- [34] J.W. Cahn, J.E. Hilliard, Free energy of a nonuniform system. I. interfacial free energy, *J. Chem. Phys.* 28 (1958) 258–267.
- [35] J.W. Cahn, On spinodal decomposition, *Acta Metall.* 9 (1961) 795–801.
- [36] R. Chella, J. Viñals, Mixing of a two-phase fluid by cavity flow, *Phys. Rev. E* 53 (1996) 3832–3840.
- [37] Y. Renardy, M. Renardy, PROST: a parabolic reconstruction of surface tension for the volume-of-fluid method, *J. Comput. Phys.* 183 (2002) 400–421.
- [38] Y.Y. Renardy, M. Renardy, V. Cristini, A new volume-of-fluid formulation for surfactants and simulations of drop deformation under shear at a low viscosity ratio, *Eur. J. Mech. B Fluids* 21 (2002) 49–59.
- [39] A. Celani, A. Mazzino, P. Muratore-Ginanneschi, L. Vozella, Phase-field model for the Rayleigh–Taylor instability of immiscible fluids, *J. Fluid Mech.* 622 (2009) 115–134.
- [40] S. Khatri, A.-K. Tornberg, A numerical method for two phase flows with insoluble surfactants, *Comput. Fluids* 49 (2011) 150–165.
- [41] Y.J. Choi, P.D. Anderson, Cahn–Hilliard modeling of particles suspended in two-phase flows, *Internat. J. Numer. Methods Fluids* 69 (2012) 995–1015.
- [42] H.G. Lee, J. Kim, A comparison study of the Boussinesq and the variable density models on buoyancy-driven flows, *J. Eng. Math.* 75 (2012) 15–27.
- [43] H.G. Lee, J. Kim, Numerical simulation of the three-dimensional Rayleigh–Taylor instability, *Comput. Math. Appl.* 66 (2013) 1466–1474.
- [44] J. Shen, X. Yang, Q. Wang, Mass and volume conservation in phase field models for binary fluids, *Commun. Comput. Phys.* 13 (2013) 1045–1065.
- [45] K.A. Smith, F.J. Solis, D.L. Chopp, A projection method for motion of triple junctions by level sets, *Interface Free Bound.* 4 (2002) 263–276.
- [46] H.G. Lee, J.-W. Choi, J. Kim, A practically unconditionally gradient stable scheme for the N -component Cahn–Hilliard system, *Phys. A* 391 (2012) 1009–1019.
- [47] H. Garcke, B. Nestler, B. Stoth, On anisotropic order parameter models for multi-phase systems and their sharp interface limits, *Physica D* 115 (1998) 87–108.
- [48] I. Steinbach, F. Pezzolla, A generalized field method for multiphase transformations using interface fields, *Physica D* 134 (1999) 385–393.
- [49] B. Nestler, A.A. Wheeler, A multi-phase-field model of eutectic and peritectic alloys: numerical simulation of growth structures, *Physica D* 138 (2000) 114–133.
- [50] B. Nestler, A.A. Wheeler, L. Ratke, C. Stöcker, Phase-field model for solidification of a monotectic alloy with convection, *Physica D* 141 (2000) 133–154.
- [51] J.R. Green, A comparison of multiphase models and techniques (Ph.D. thesis), The University of Leeds, Leeds, 2007.
- [52] H.G. Lee, J. Kim, A second-order accurate non-linear difference scheme for the N -component Cahn–Hilliard system, *Phys. A* 387 (2008) 4787–4799.
- [53] L. Vanherpe, F. Wendler, B. Nestler, S. Vandewalle, A multigrid solver for phase field simulation of microstructure evolution, *Math. Comput. Simulation* 80 (2010) 1438–1448.
- [54] H.G. Lee, J. Kim, An efficient and accurate numerical algorithm for the vector-valued Allen–Cahn equations, *Comput. Phys. Commun.* 183 (2012) 2107–2115.
- [55] I. Steinbach, F. Pezzolla, B. Nestler, M. Seeßelberg, R. Prieler, G.J. Schmitz, J.L.L. Rezende, A phase field concept for multiphase systems, *Physica D* 94 (1996) 135–147.
- [56] J.W. Cahn, J.E. Taylor, Surface motion by surface diffusion, *Acta Metall.* 42 (1994) 1045–1063.
- [57] F.H. Harlow, J.E. Welch, Numerical calculation of time-dependent viscous incompressible flow of fluid with free surface, *Phys. Fluids* 8 (1965) 2182–2189.
- [58] H.G. Lee, K. Kim, J. Kim, On the long time simulation of the Rayleigh–Taylor instability, *Internat. J. Numer. Methods Engrg.* 85 (2011) 1633–1647.
- [59] U. Trottenberg, C. Oosterlee, A. Schüller, *Multigrid*, Academic Press, London, 2001.
- [60] P. Yue, C. Zhou, J.J. Feng, Spontaneous shrinkage of drops and mass conservation in phase-field simulations, *J. Comput. Phys.* 223 (2007) 1–9.
- [61] L.D. Landau, E.M. Lifshitz, *Fluid Mechanics*, Butterworth-Heinemann, Oxford, 1987.
- [62] G.A. Greene, J.C. Chen, M.T. Conlin, Onset of entrainment between immiscible liquid layers due to rising gas bubbles, *Int. J. Heat Mass Transfer* 31 (1988) 1309–1317.
- [63] L. Rayleigh, Investigation of the character of the equilibrium of an incompressible heavy fluid of variable density, *Proc. Lond. Math. Soc.* 14 (1883) 170–177.
- [64] G. Taylor, The instability of liquid surfaces when accelerated in a direction perpendicular to their planes. I, *Proc. R. Soc. A* 201 (1950) 192–196.
- [65] H.G. Lee, J. Kim, Regularized Dirac delta functions for phase field models, *Internat. J. Numer. Methods Engrg.* 91 (2012) 269–288.
- [66] J.M. Park, P.D. Anderson, A ternary model for double-emulsion formation in a capillary microfluidic device, *Lab Chip* 12 (2012) 2672–2677.